Indian Journal of Pure & Applied Physics
Vol. 64, May 2026, pp. 491-501
DOI: 10.56042/ijpap.v65i5.27239

Cumulative Effect of Post-Deposition Annealing and Elevated Substrate Temperature On Structural, Electrical, Optical Properties and Wettability of RF-Sputtered ITO Thin Films

Abhimanyu[a, b], Vikas[a, b], Neelam Kumari[a] & Mukesh Kumar[a, b*]

[a]CSIR-Central Scientific Instruments Organisation, Chandigarh 160 030, India

[b]Academy of Scientific and Innovative Research (AcSIR), Ghaziabad 201 002, India

Received: 4th January 2026; accepted: 30th March 2026

In this study, the influence of substrate temperature and post-deposition annealing on the structural, electrical, and optical properties of indium tin oxide (ITO) thin films has been systematically investigated. ITO films were deposited using an RF magnetron sputtering system at varying substrate temperatures. The as-deposited films revealed that higher substrate temperatures lead to enhanced crystallinity, improved electrical conductivity, and greater optical transparency. Furthermore, post-deposition annealing of room-temperature-grown films resulted in an increase in visible transmittance from 77 % to 82 %, accompanied by a rise in sheet resistance from 30 to 70 Ω/sq. Comparative analysis indicated that films directly deposited at elevated substrate temperatures exhibit superior performance, achieving visible transparency of approximately 85 % and a lower sheet resistance of around 33 Ω/sq, outperforming their annealed counterparts.

Keywords: Indium tin oxide (ITO), RF magnetron sputtering, Substrate temperature, Annealing

1 Introduction

Transparent conducting oxide (TCO) thin films are integral to emerging electronic and optoelectronic technologies due to their unique combination of high optical transparency and electrical conductivity. Their use enables compact, low-power and fast-response devices, making TCOs essential for next-generation systems. Currently, TCO films play a critical role in a wide range of applications including solar cells, transparent heaters, liquid-crystal displays and low-emissivity infrared-reflective coatings[1]. Among the available n-type TCO materials such as indium tin oxide (ITO), fluorine-doped tin oxide (FTO), and aluminum-doped zinc oxide (AZO), ITO is particularly preferred owing to its superior conductivity, high visible transparency, excellent chemical stability, strong mechanical durability, and UV absorption capability[2,3]. Although both chemical and physical deposition methods are used for TCO fabrication, physical vapour deposition techniques such as electron-beam evaporation, pulsed-laser deposition, and sputtering are favoured for their cleaner processes and better control over film properties[4–6]. In particular, sputtering systems are widely adopted at industrial scale due to their precise tunability of process parameters, enabling fine control of thin-film characteristics. In the present study, ITO films were deposited by RF magnetron sputtering for investigations of their structural, electrical and optical properties in different deposition and post-deposition environments.

Effect of deposition parameters such as RF power, substrate temperature, oxygen partial pressure and post-deposition annealing on the structural, electrical and optical performance of ITO films has been extensively investigated in previous studies[7–10]. The effects of different annealing techniques, such as rapid infrared annealing and conventional furnace annealing, and the effect of UV nanosecond laser annealing on ITO films have also been studied[11-12]. Most of these studies have primarily emphasized on thermal treatment of ITO films, either during deposition or through post-deposition annealing. However, a systematic comparative analysis of these temperature treatments has not yet been reported. In the present work, the properties of ITO films, deposited at elevated temperature (250 °C), have been compared with those of the films deposited at room-temperature and subsequently subjected to post-deposition annealing (at 300 °C).

*Corresponding author: E-mail: mukeshk@csio.res.in

2 Materials and Methods

2.1 Film deposition

ITO thin films were deposited on 2.5 cm × 2.5 cm glass substrates using an RF magnetron sputtering system (Make: HHV, India). A cylindrical ITO target with a diameter of 6” and a thickness of 6 mm, was used for deposition. The target composition consisted of In_2O_3: SnO_2 in a 90:10 ratio with 99.99 % purity. Prior to deposition, the glass substrates were ultrasonically cleaned using isopropanol (IP), loaded into the sputtering chamber and evacuated to a base pressure of 1.8×10^{-6} mbar. Argon was then introduced as the sputtering gas at a controlled flow rate of 42 sccm using a mass flow controller. The RF power was gradually increased in steps of 10 W up to a maximum of 450 W, with a ramping rate of approximately 100 W/min. To remove surface contamination, the target was pre-sputtered for 10 minutes before initiating the actual deposition. The process pressure was maintained at 1.4×10^{-2} mbar. Film deposition was carried out at two different substrate temperature, i.e. at room temperature and at 250 °C. For deposition at 250 °C, the deposition duration ranged from 30 to 90 minutes for different film thickness, whereas for room-temperature films, deposition duration of 90 and 135 minutes were used.

2.2 Characterization

The electrical properties of the ITO films were evaluated using a four-point probe system (Make: Ossila) and a Hall effect measurement setup (HMS-7000). Optical transmission spectra were recorded using a UV–Vis–NIR spectrophotometer (Agilent Technologies, Cary 7000), while film thickness was measured using a Thin Film Analyser (Filmetrics FT10-RT). The structural characteristics were analyzed by X-ray diffraction (XRD) using a Bruker D8 Advance diffractometer with Cu Kα radiation, over a 2θ range of 20–65°. Surface topography was examined using a Coherence Correlation Interferometer (CCI) (Taylor-Hobson). Morphological features and elemental composition were investigated through field-emission scanning electron microscopy (FE-SEM, HITACHI) equipped with an energy-dispersive X-ray (EDX) detector.

2.3 Thermal Annealing Process

The Room-temperature deposited films were thermally annealed at 300 °C for durations of 30 and 120 minutes. The annealing chamber temperature was raised from ambient to 300 °C over approximately 25 minutes and annealing was carried out under atmospheric conditions. The influence of post-deposition annealing on film performance was compared with that of high-temperature deposition to assess the changes in structural, electrical, and optical properties.

3 Results and Discussion

3.1 Thickness Measurement

The thicknesses of the deposited ITO films, measured using spectrophotometer, cross-sectional FE-SEM, and CCI, are summarized in Table 1. Representative thickness measurements obtained from FE-SEM and CCI are shown in Fig. 1. The variation in thickness across measurement methods was within ±20 nm. For further calculations, cross-sectional FE-SEM values were used, as they provide the most direct physical measurement.

Thickness of the ITO films was determined by using optical reflection and transmittance data (acquired by Thin Film Analyser) and by fitting modelled transmittance and reflectance spectra using a four-layer structure (air / ITO / glass / air). The refractive indices of air and glass were set to 1.0 and 1.52, respectively. The optimized refractive index and

Table 1 — Thicknesses of the ITO films (in nm) measured through different techniques

Sample Name	Sample ID	Thin Film Analyser	FE-SEM	CCI
film deposited at 250°C for a sputtering duration of 30 min	250°C_30min	128	124	128
film deposited at 250°C for a sputtering duration of 60 min	250°C_60min	187	187	194
film deposited at 250°C for a sputtering duration of 90 min	250°C_90min	310	310	332
film deposited at room-temperature for a sputtering duration of 90 min	RT_90min	472	468	475
film deposited at room-temperature for a sputtering duration of 135 min	RT_135min	695	719	704

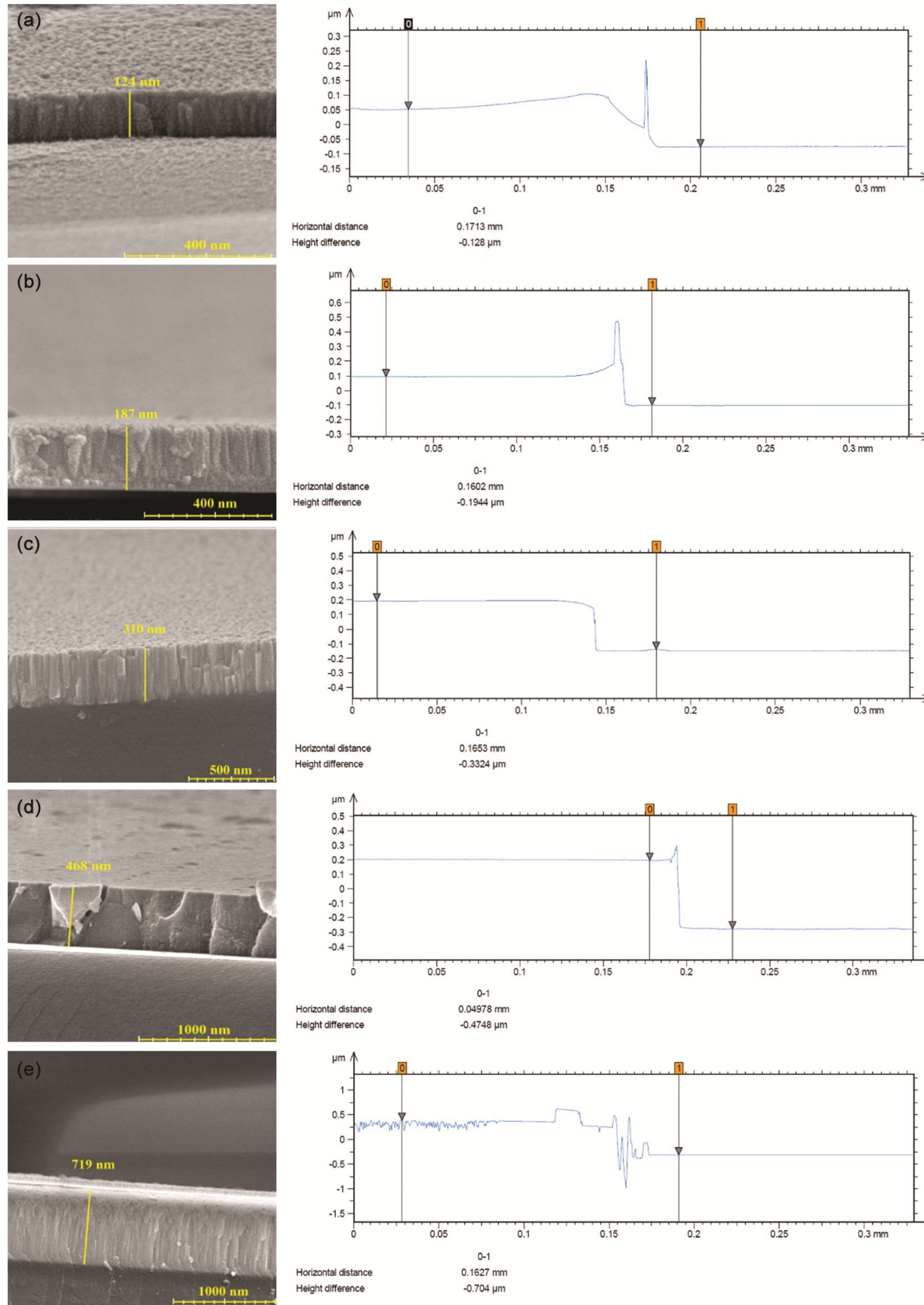

Fig. 1 — Thickness measurement of ITO films by Cross-sectional SEM (on left) and by CCI (on right) (a) film deposited at 250°C for a duration of 30 min (250°C_30min) (b) film deposited at 250°C for a duration of 60 min (250°C_60min) (c) film deposited at 250°C for a duration of 90 min (250°C_90min) (d) film deposited at room-temperature for a duration of 90 min (RT_90min); and (e) film deposited at room-temperature for a duration of 135 min (RT_135min)

extinction coefficient of ITO were estimated to be ~2.1 and ~0.01 at 632.8 nm, respectively.

3.2 Structural Properties

The structural properties of the ITO films were characterised using XRD analysis. Figure 2 shows the XRD patterns of as-deposited and annealed films. Room-temperature (RT) deposited samples exhibit a predominantly amorphous structure with a broad feature near 32°, indicating weak ordering towards the (222) plane as shown in Fig. 2 (a) (Sample RT_135min). Increasing the substrate temperature

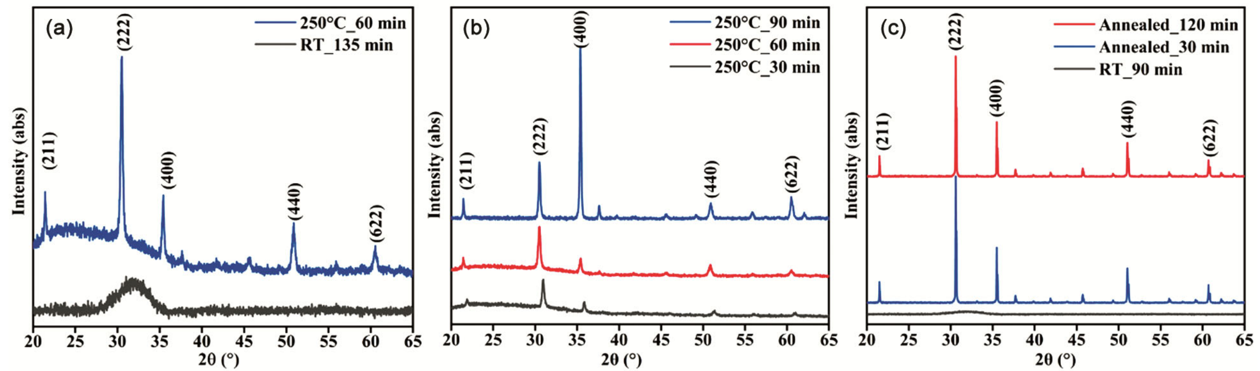

Fig. 2 — XRD pattern of (a) RT_135 min & 250°C_60 min, (b) film deposited at 250°C for 30, 60 & 90 minutes (250°C_30 min, 250°C_60 min, & 250°C_90 min), (c) room temperature deposited (RT_90 min) and subsequently annealed films (Annealed_120 min and Annealed_30 min)

promotes crystallisation, resulting in polycrystalline films with preferred (222) orientation at lower thicknesses as shown in Fig. 2 (b). With increasing film thickness at 250°C, the preferred orientation shifts toward the (400) plane, consistent with literature reporting enhanced surface mobility of adatoms, favouring low-index crystallographic planes[13].

Annealing of films deposited at room temperature improves crystallinity, as evident from increased (222) peak intensity. Longer annealing times facilitate atomic diffusion and grain reorganization toward lower-energy configurations. Figure 2 (c) illustrates the enhancement in crystallinity of the room-temperature deposited films after annealing. The (222) diffraction peak intensity increases significantly upon annealing, indicating improved crystal ordering. All observed peaks match well with the standard ICDD reference file (00-065-0688), confirming the polycrystalline cubic bixbyite structure of ITO. The increase in peak intensity reflects enhanced grain growth and reduction of structural disorder. With longer annealing durations, atomic diffusion and rearrangement promote a transition toward a lower surface-energy configuration[14], similar to that observed in high-temperature, low-thickness deposited films.

The full width at half maximum (FWHM), diffraction angle (2θ), crystallite size calculated using the Scherrer equation (β: FWHM, D: crystallite size, d: interplanar spacing, a: lattice constant), micro-strain ε [15] and Dislocation density δ (number of lines per nm^2) are summarized in Table 2, along with the average visible transmittance (T %). Both higher deposition temperature and post-deposition annealing lead to an increase in crystallite size, confirming significant improvement in film crystallinity. The room temperature deposited films had high micro strain and dislocation density, which decreased on annealing, as well as for the high temperature deposited films.

3.3 Electrical Property

The electrical properties of the ITO films were evaluated using a four-point probe system to measure the sheet resistance and a Hall effect setup to determine the carrier characteristics, respectively. A clear reduction in sheet resistance was observed with increasing film thickness. Films deposited at higher substrate temperature exhibited significantly lower sheet resistance compared to those deposited at room temperature, which is attributed to their enhanced crystallinity. Improved crystallinity reduces defect density and minimizes carrier scattering, thereby enhancing conductivity[16]. For the high-temperature deposited samples, sheet resistance values decreased appreciably from 169 Ω/sq. (250°C_30 min) to 79 Ω/sq. (250°C_60 min) and 35 Ω/sq. (250°C_90 min).

In contrast, post-deposition annealing led to an increase in sheet resistance relative to the as-deposited room-temperature films, with values rising from 28 Ω/sq. to approximately 62 Ω/sq. (for annealing duration of 30 min) and 67 Ω/sq. (for annealing duration of 120 min) as measured from Four Probe. This increase is attributed to the reduction in oxygen vacancy concentration during annealing in ambient atmosphere[17]. As reported earlier, oxygen vacancies act as donor defects in oxide films and primarily contribute to charge transport in as-deposited ITO [18]. During annealing, oxygen incorporation into the films fills these vacancies, lowering the carrier concentration and consequently increasing the sheet resistance.

Table 2 — FWHM β, Crystallite size D (in nm), highest peak angle 2θ, interplanar spacing d, crystal lattice constant a, Micro-strain ε, Dislocation density δ, and average visible transmittance T% of the as deposited and annealed films

Sample	β (°)	D (nm)	2θ (°)	d (Å)	a(Å)	ε	δ (×10^{-3}) nm^{-2}	T%
250°C_30 min	0.28	29.77	30.49	2.93	10.14	0.0044	1.128	85.18
250°C_60 min	0.28	29.81	30.49	2.93	10.14	0.0044	1.125	82.96
250°C_90 min	0.19	44.73	35.38	2.53	10.13	0.0026	0.499	88.53
RT_135 min	4.18	19.60	32.20	2.78	9.62	0.0632	2.603	79.72
RT_90 min	5.91	13.80	31.04	2.88	9.97	0.0928	5.251	77.54
Annealed_30 min	0.10	95.24	30.60	2.92	10.11	0.0016	0.110	82.80
Annealed_120 min	0.09	97.17	30.60	2.92	10.11	0.0016	0.106	82.17

Table 3 — Hall Measurement Data

Sample	Carrier conc. (cm^{-3})	$R_{S\,(Hall)}$ (Ω/sq.)	$R_{S\,(four\ probe)}$ (Ω/sq.)	Resistivity (Ω-cm)	Conductivity (S-cm^{-1})	Mobility (cm^2/V-s)
250°C_30 min	3.70E+19	167.81	169	2.03E-03	4.92E+02	8.31419
250°C_60 min	4.93E+19	76.72	79	6.14E-04	1.63E+03	20.6608
250°C_90 min	1.94E+20	30.36	35	4.94E-04	2.02E+03	65.001
RT_135 min	1.11E+20	25.95	28	1.82E-03	5.51E+02	31.028
RT_90 min	2.80E+20	32.71	39	1.57E-03	6.36E+02	14.162
Annealed_30 min	1.67E+20	61.93	62	2.85E-03	3.51E+02	13.115
Annealed_120 min	1.57E+20	70.61	67	3.31E-03	3.02E+02	11.995

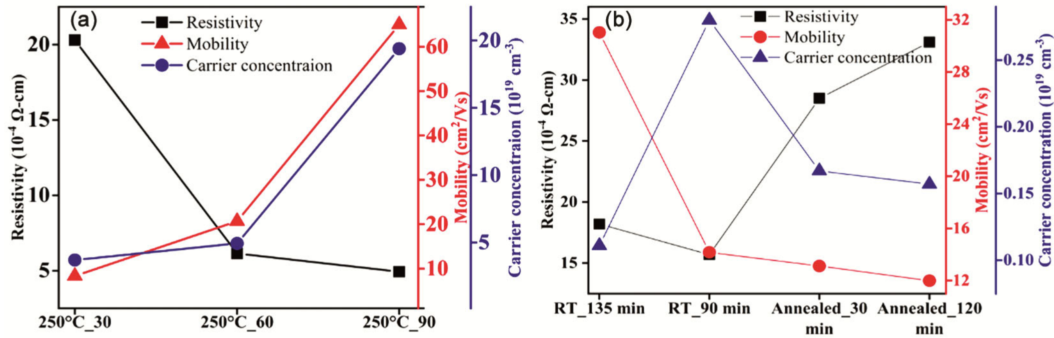

Fig. 3 — Resistivity, mobility and carrier concentration of samples deposited (a) at 250°C (250°C_30min, 250°C_60min and 250°C_90min) and (b) at room temperature (RT_135min, RT_90min) and subsequently annealed (Annealed_30min, Annealed_120min)

Table 3 summarizes the carrier concentration, resistivity, and mobility values obtained from Hall effect measurements. The sheet resistance calculated from the Hall data shows good agreement with the values measured using the four-point probe system, confirming the reliability of the electrical characterization.

Hall effect measurements revealed that the carrier concentration of the as-deposited films increased with increasing film thickness for both room-temperature and 250 °C depositions (Figure 3). Carrier mobility also improved with thickness, which can be attributed to enhanced crystallinity and reduced defect scattering. The highest mobility 65 cm^2/V-s was observed for the film deposited at 250°C for 90 minutes. Previous studies have shown that ITO films, exhibiting a preferred (400) orientation, generally possess higher mobility[19]. The combined improvement in mobility and carrier concentration contributes to the observed reduction in sheet resistance for thicker and high-temperature deposited films.

In contrast, a notable decrease in carrier concentration occurred upon annealing the room-temperature deposited films. This reduction is associated with the suppression of oxygen vacancy donors due to oxygen incorporation from the ambient atmosphere during annealing[17]. Consequently, both carrier concentration and mobility declined, leading to an increase in sheet resistance—from 30 Ω/sq. in the as-deposited state to 62 Ω/sq. and 71 Ω/sq. after annealing for 30 and 120 minutes, respectively.

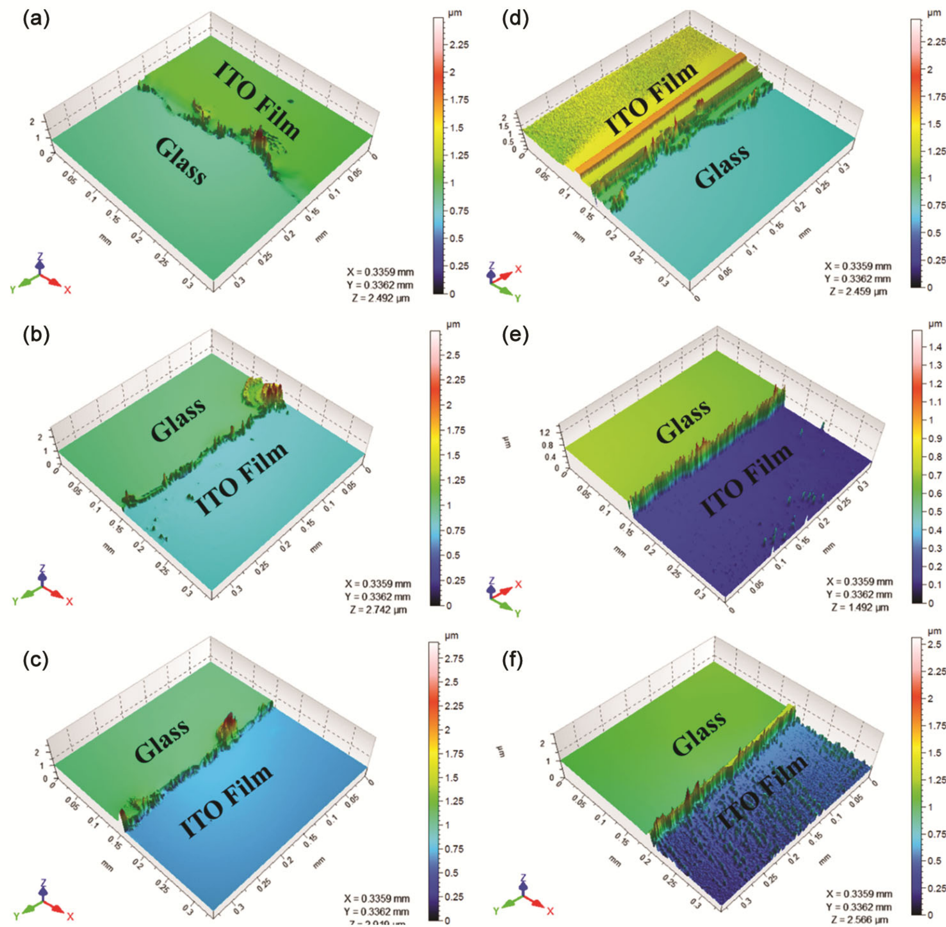

Fig. 4 — Optical surface morphology of (a) 250°C_30 min, (b) 250°C_60 min, (c) 250°C_90 min, (d) RT_90 min and annealed films (e) annealed_30 min, (f) annealed_120 min

Similar trends in carrier transport properties following high-temperature annealing of room-temperature deposited ITO have been reported earlier in the literature, where annealing temperatures as high as 480 °C were used [20].

3.4 Optical Surface Morphology

The surface morphology of the films was examined using CCI instrument, focusing on the step-edge region to assess glass-ITO interface characteristics. As shown in Fig. 4, the as-deposited films exhibited smooth surfaces regardless of the substrate temperature. However, post-deposition annealing resulted in a noticeable increase in surface roughness. Similar behaviour has been reported[21] where annealing induced grain growth and surface texturing, leading to higher roughness values. The increase in roughness can subsequently influence both the optical transmittance and protective performance of the films, as discussed later in this work.

3.5 Optical Properties

Figure 5 presents the optical transmission spectra of the ITO films. All samples exhibit high transparency in the visible region, with average transmittance values of approximately 77% for room-temperature deposited films and around 85 % for those deposited at 250 °C (Figure 5 (a)). An increase in substrate temperature leads to a further enhancement in visible transmittance, which is consistent with improved crystallinity and reduced light scattering. However, a reduction in near-infrared (NIR) transmittance is observed with increasing film thickness and deposition temperature (Figures 5 (a) & (b)). This decrease is attributed to higher free-carrier absorption at elevated carrier concentrations[22]. As per Drude model, an increase in carrier concentration shifts the plasma wavelength toward shorter wavelengths, thereby reducing NIR transparency. The plasma wavelength given by the Drude model is given as

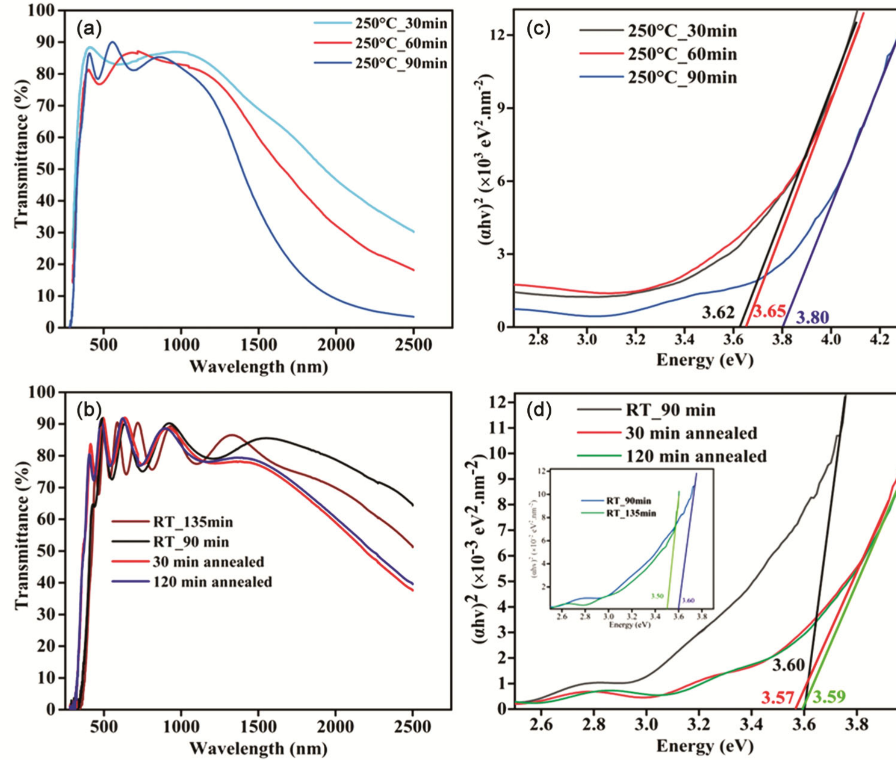

Fig. 5 — Optical properties of ITO films: (a) & (b) transmittance and (c) & (d) band gaps of films

$$\lambda_p = 2\pi c\sqrt{\frac{\varepsilon m^*}{ne^2}} \qquad \ldots (1)$$

where n is the charge carrier concentration in the film, e is the electronic charge, m* is the effective mass, and ε is the permittivity.

In ITO films, the plasma wavelength is inversely proportional to the square root of the carrier concentration. Therefore, an increase in carrier concentration shifts the plasma wavelength toward shorter values, which consequently reduces near-infrared transmittance. A corresponding shift in the absorption edge toward lower wavelengths was observed for the high-temperature deposited films with increasing thickness, indicating a widening of the optical band gap, as shown in Fig. 5 (c). This band gap broadening can be attributed to the Burstein–Moss effect, wherein the filling of lower-energy conduction band states by excess carriers leads to an apparent increase in the band gap [1]. A similar behaviour is observed in the annealed films Fig. 5 (d); however, due to a slight decrease in carrier concentration after annealing, a marginal reduction in the band gap occurs. Overall, the band gap of the room-temperature deposited films remains comparable to that of the annealed samples.

A comparison of the optical properties of the as-deposited and annealed films is also presented in Fig. 5 (b). The average visible transmittance of the as-deposited film was approximately 77 %, which increased to 81 % and 82 % after annealing for 30 and 120 minutes, respectively (Table 2). This improvement in visible transmittance is attributed to the enhanced crystallinity of the ITO films induced by annealing[23]. However, a reduction in near-infrared (NIR) transmittance was noted in the annealed samples. This decrease may be associated with increased surface roughness, as confirmed by optical surface morphology measurements, leading to enhanced scattering of NIR light. Furthermore, previous studies have reported reduced NIR transmittance in films with higher inter-crystalline scattering[24]. Thus, an increase in crystallinity may also introduce more grain boundaries, contributing to additional NIR scattering. A similar mechanism can explain the optical behaviour observed in high-temperature deposited films.

3.6 Morphological Analysis

Figure 6 (a-c) presents the FE-SEM images of the films deposited at 250 °C for 30, 60, and 90 minutes. All ITO films exhibited a crystalline microstructure,

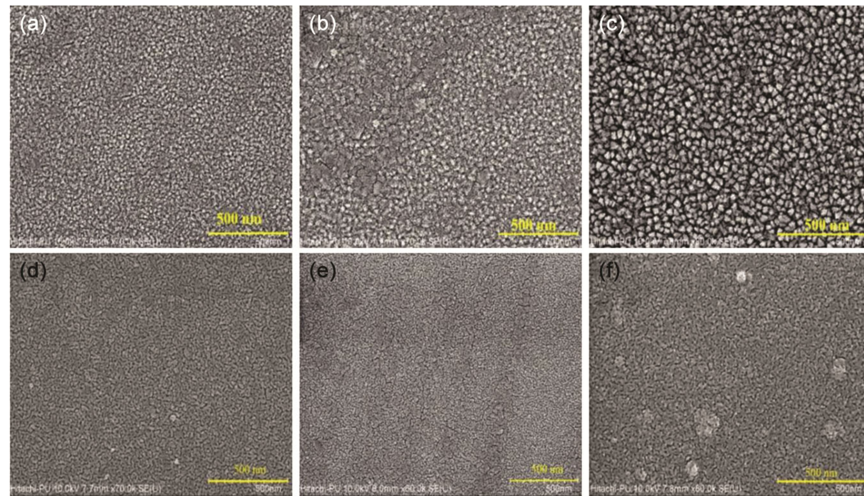

Fig. 6 — FE-SEM images for surface morphology of ITO films (a-c) for films deposited at 250 °C (250 °C_30min, 250 °C_60min and 250 °C_90min respectively) and (d-f) for room temperature deposited and annealed films (annealed_30 min and annealed_120 min respectively)

with grain size and crystallinity increasing as the film thickness increased. These observations are consistent with the XRD results, which showed enhanced peak intensity and reduced FWHM with longer deposition durations. The progressive grain growth observed in the SEM images contributes to the reduction in sheet resistance due to decreased grain boundary scattering[25].

For the room-temperature deposited films, the initial morphology was smooth and predominantly amorphous. Upon annealing, the films transformed into a polycrystalline structure, as also shown in Fig. 6 (d-f). The annealed samples exhibited the formation of island-like features, which became more pronounced with increasing annealing time. This behaviour is characteristic of the Volmer–Weber growth mode, where discontinuous islands form during nucleation. Cross-sectional FE-SEM images further confirmed the columnar microstructure of the films, supporting the island coalescence mechanism during annealing. Although the annealed films attained a polycrystalline phase, they did not exhibit the porous morphology observed in the films deposited at 250 °C.

3.6.1 EDX Analysis

Energy-dispersive X-ray spectroscopy (EDX) was performed using the inbuilt detector of the FE-SEM system. The corresponding spectra (Figure 7) confirm the elemental composition of the ITO films, and the quantified atomic percentages are summarized in Table 4.

The EDX results show that, for samples deposited at higher temperatures, both Sn and O concentrations decreased with increasing deposition time. This observation indicates the formation of additional oxygen vacancies at longer deposition durations. The higher oxygen vacancy concentration enhances the free carrier density, leading to a reduction in sheet resistance.

It is well understood that oxygen vacancies contribute significantly to the carrier concentration in as-deposited ITO films. In contrast, Sn incorporation either through substitutional or interstitial doping contributes fewer carriers, as each Sn atom donates one carrier while each oxygen vacancy donates two. Therefore, even though the Sn atomic fraction decreases, the increased oxygen vacancy concentration compensates for the reduced Sn doping, resulting in an overall decrease in sheet resistance.

For the room-temperature deposited samples (RT_90 min and RT_135 min), the In atomic percentage decreased, while Sn and O increased slightly. This suggests a reduction in oxygen vacancy concentration, consistent with Hall measurements showing a lower carrier concentration for RT_135 min compared to RT_90 min. Nevertheless, the sheet resistance continued to decrease due to enhanced carrier mobility associated with increasing film thickness. Annealed samples showed negligible variation in elemental composition, which explains the nearly identical sheet resistance values between them.

3.7 Wettability Studies

To evaluate wettability of deposited ITO films, contact angle (CA) measurements were performed, and the results are summarized in Table 5. For room-

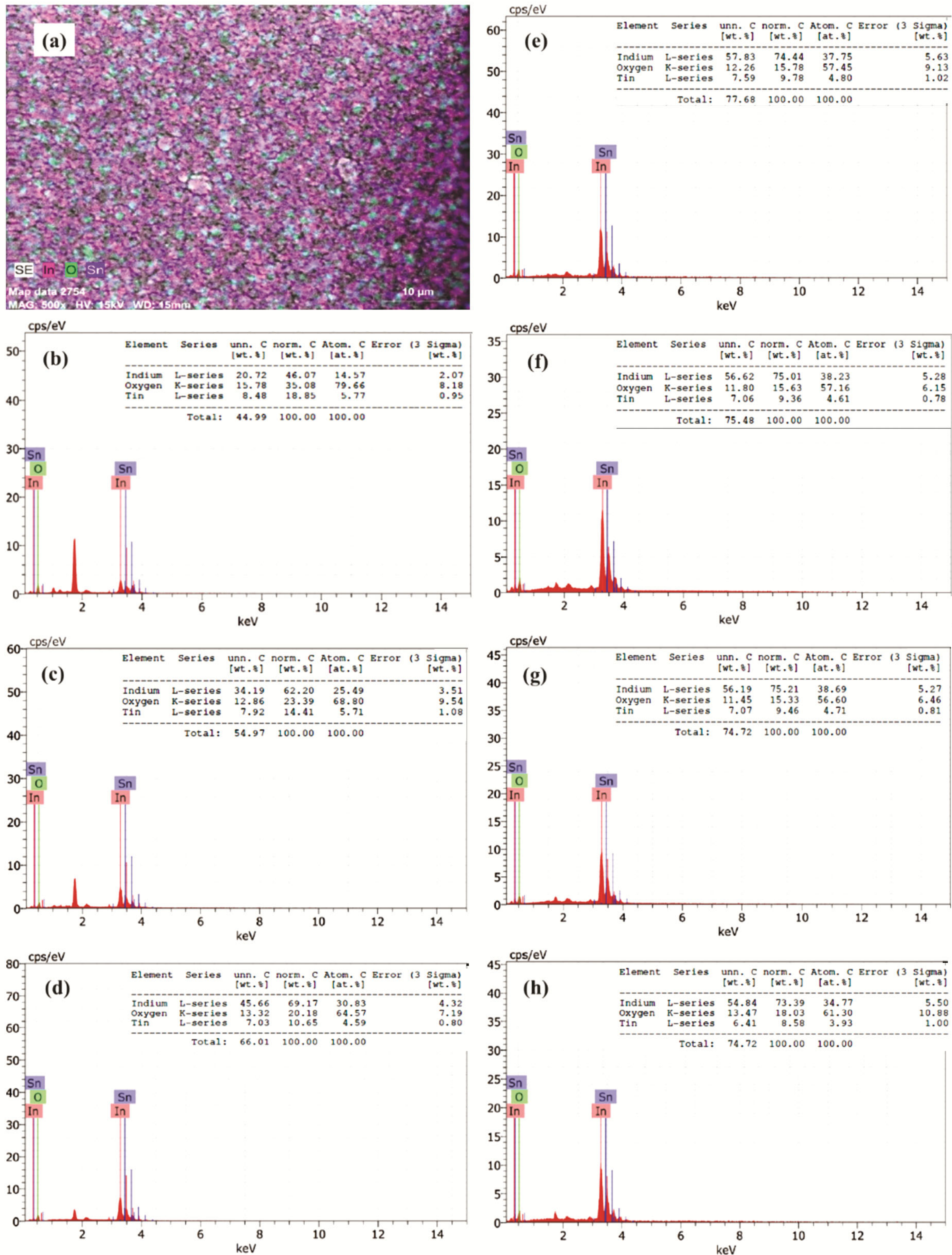

Fig. 7 — (a) Elemental mapping in RT_135 min film and concentrations of the (b) 250°C_30min (c) 250°C_60min (d) 250°C_90min, (e) RT_135min, (f) RT_90min, (g) annealed_30min and (h) annealed_120min films

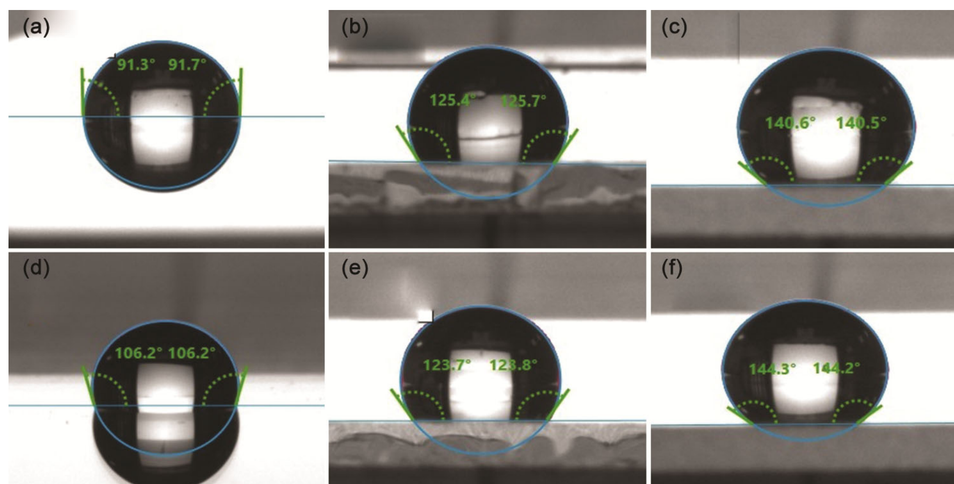

Fig. 8 — Contact angle measurement of ITO films (a) 250°C_30 min; (b) 250°C_60 min; (c) 250°C_90 min; (d) RT_90 min; (e) annealed_120 min; and (f) annealed_30 min

Table 4 — Atomic percentages of ITO samples obtained from EDX

Sample ID	Indium (at. %)	Oxygen (at. %)	Tin (at. %)
250°C_30min	14.57	79.66	5.77
250°C_60min	25.49	68.8	5.71
250°C_90min	30.83	64.57	4.59
RT_90min	38.23	57.16	4.61
RT_135min	37.75	57.45	4.80
Annealed_30min	38.69	56.6	4.71
Annealed_120min	34.77	61.3	3.93

Table 5 — Water contact angle of the ITO samples

Sample	Contact angle (°)
Bare glass	45.6
250°C_30 min	91.5
250°C_60 min	125.5
250°C_90 min	140
RT_135 min	105-108
RT_90 min	106-108
Annealed_30 min	144-150
Annealed_120 min	123-125

temperature deposited films, the average contact angle was found to be approximately 106 ° (Figure 8), and no significant variation in CA was observed with increasing film thickness. In contrast, films deposited at 250 °C exhibited a clear dependence of CA on deposition time: a 30-minute film showed a contact angle of 92 °, which increased to 125 ° for a 60-minute deposition and further to 135 ° for 120 minutes. Hydrophobicity of such TCOs is a desirable feature for optoelectronic devices in humid or underwater environments[26].

Annealing resulted in an increase in contact angle, with the sample annealed for 30 minutes exhibiting a contact angle of 145 °, while the 120-minute annealed sample showed a slightly lower value of 124 °. This enhancement in hydrophobicity is attributed to increased surface roughness, which traps air within the film and prevents water molecules from interacting directly with the ITO surface[21]. Thus, the hydrophobic nature of the films can be improved either by increasing the deposition temperature or by post-deposition annealing of room-temperature-deposited films.

4 Conclusion

In the current study, ITO films were deposited on glass substrates under a range of processing conditions and their structural, optical, electrical and surface characteristics were systematically evaluated. Structural investigations revealed that films deposited at room temperature were predominantly amorphous, whereas those deposited at elevated temperatures or subjected to post-deposition annealing exhibited polycrystalline nature. This transition was further corroborated by morphological analysis, which also indicated a reduction in lattice distortion with increasing temperature. Electrical measurements demonstrated that films deposited at higher temperatures possess lower sheet resistance compared to their room-temperature counterparts, attributable to improved crystallinity and enhanced carrier mobility. In contrast, annealing in ambient atmosphere led to an increase in sheet resistance, likely due to oxygen incorporation and reduced carrier concentration.

Optical characterization showed that films deposited at elevated temperatures exhibited enhanced average visible transmittance along with improved conductivity as deposition time increased, while a concomitant reduction in near-infrared (NIR) transmittance was observed. However, room-temperature-deposited films maintained a relatively stable visible transmittance of approximately 80 %. Upon annealing, these films exhibited a modest increase in visible transmittance accompanied by an increase in sheet resistance, reaching values of ~65 Ω/sq across all annealed samples. Surface wettability studies indicated that both high-temperature-deposited films and annealed room-temperature films exhibit hydrophobic behaviour. Furthermore, hydrophobicity was found to increase with deposition time for high-temperature films and with annealing duration for room-temperature films, suggesting a correlation with surface morphology evolution.

In summary, films deposited at elevated temperatures are well-suited for applications demanding high visible transparency and low electrical resistance, such as transparent electrodes and heaters. Their inherent hydrophobicity further supports stable operation under humid conditions. Conversely, for applications requiring higher NIR transparency, room-temperature-deposited films are more appropriate. Annealed room-temperature films may also be considered for heating applications, as their optical and electrical properties exhibit minimal variation after moderate annealing durations, indicating good thermal stability.

Acknowledgement

The Authors are thankful to the UGC, New Delhi, India, for providing financial support for this work as a UGC-JRF fellowship (code number 191620039986).

References

1 Gordon R G, Criteria for Choosing Transparent Conductors, MRS Bull, 25 (8) (2000) 52.
2 Txintxurreta J, G-Berasategui E, Ortiz R, Hernández O, Mendizábal L & Barriga J, *Coatings*, 11 (1) (2021) 1.
3 Ren N, Shi P, Sheng Z, Zhong K, Du H, Shan Q, Zhu J, Li T & Ban S, *Solar Energy*, 203 (2020) 240.
4 Prepelita P, Stavarache I, Craciun D, Garoi F, Negrila C, Sbarcea B G & Craciun V, *Beilstein J Nanotechnol*, 10 (2019)1511.
5 Lu Y, Wang S, Yang M, Xu X & Li Q, *J Mater Sci: Mater Electron*, 29 (20) (2018) 17525.
6 Nuchuay P, Chaikeeree T, Horprathum M, Mungkung N, Kasayapanand N, Oros C, Limwichean S, Nuntawong N, Chananonnawathorn C, Patthanasettakul V, Muthitamongkol P, Samransuksamer B, Denchitcharoen S, Klamchuen A, Thanachayanont C & Eiamchai P, *Current Appl Phys*, 17 (2) (2017) 222.
7 Txintxurreta J, G-Berasategui E, Ortiz R, Hernández O, Mendizábal L & Barriga J, *Coatings*, 11 (1) (2021) 1.
8 Du H, Lv M, Meng J & Zhu W, *Appl Opt*, 55 (34) (2016) D115.
9 Wen L, Sahu B B, Yeom G Y & Han J G, *Vacuum*, 193 (2021) 110520.
10 Robb A J, Duca Z A, White N, Woodell P & Ward P A, *Thin Solid Films*, 788 (2024) 140152.
11 Li J, Jiang L, Li X, Luo J, Liu J, Wang M & Yan Y, *Mater*, 16 (10) (2023) 3803.
12 Münzer A, Weittenhiller M, Bivour M, Meyer F & Glunz S W, *Thin Solid Films*, 825 (2025) 140743.
13 Chen Q, Gong T, Chen W, Fang F, Feng Y, Chen S, Liu D & Liu T, *Ceram Int*, 51 (2025) 3163.
14 Chen Y, Zhou Y, Zhang Q, Zhu M & Liu F, *J Mater Sci: Mater Electron*, 18 (2007) 411.
15 Anandan R, Rajendran J & Piraviperumal M, *ACS Appl Electron Mater*, 4 (2022) 5506.
16 Oh M S & Seo I, *J Korean Phys Soc*, 71 (2) (2017) 101.
17 Lu Y, Wang S, Yang M, Xu X & Li Q, *J Mater Sci: Mater Electron*, 29 (20) (2018) 17525.
18 Afre R A, Sharma N, Sharon M & Sharon M, *Rev Advanced Mater Sci*, 53 (2018) 79.
19 Bhorde A, Jadhavar A, Waykar R, Nair S, Borate H, Pandharkar S, Aher R, Naik D, Vairale P, Lonkar G & Jadkar S, *Thin Solid Films,* 704 (2020) 137972.
20 Kim Y, Joo S H, Shin S G, Choi H W, Bark C W, Rim Y S, Kim K H & Kim S, *Coatings* 12 (2) (2022) 203.
21 Cho Y C, Cha S Y, Shin J M, Park J H, Park S E, Cho C R, Park S, Pak H K, Jeong S Y & Lim A R, *Solid State Commun*, 149 (15) (2009) 609.
22 Lacroix B, Santos A J, Hurand S, Corvisier A, Paumier F, Girardeau T, Maudet F, Dupeyrat C, García R & Morales F M, *J Phys Chem C*, 123 (22) (2019) 14036.
23 Hamzah N A, Asri R I M, Ahmad M A, Md Sahar M A A Z, Waheeda S N & Hassan Z, *J Phys: Confer Ser*, Institute of Physics Publishing, 1535 (2020) 012036.
24 Prepelita P, Stavarache I, Craciun D, Garoi F, Negrila C, Sbarcea B G & Craciun V, *Beilstein J Nanotechnol*, 10 (2019) 1511.
25 Kerkache L, Layadi A, Dogheche E & Rémiens D, *EPJ Appl Phys*, 39 (1) (2007) 1.
26 SRS Praveen Kumar V, Kumar M, Kumari N, Sharma A L, *Appl Opt*, 59 (2) (2020) 564.